Unravelling the impact of electroconductivity on metal plating position in redox-active electrolytes

Seyoung Lee [a,1], Youngjae Jung [a,1], Jihun Cho [a], Dowan Kim [a], Hyeonseok Lee [a], Seohae Kim [a], Hyo Jin [a], Hyeji Min [a], Wang-Geun Lee [b], Youngsik Kim [a], Stefano Passerini [c,d,e,*], Yongil Kim [f,*]

[a] School of Energy and Chemical Engineering, Ulsan National Institute of Science and Technology (UNIST), UNIST-gil 50, Ulsan, 44919, South Korea
[b] Department of Chemical Engineering, Myongji University, Yongin-si, Gyeonggi-do, 17058, South Korea
[c] Helmholtz Institute Ulm (HIU), Helmholtzstrasse 11, 89081, Ulm, Germany
[d] Karlsruhe Institute of Technology (KIT), P.O. Box 3640, 76021, Karlsruhe, Germany
[e] Austrian Institute of Technology, Giefinggasse 4, 1210, Wien, Austria
[f] School of Chemical, Biological and Battery Engineering, Gachon University, Seongnam-si, Gyeonggi-do, 13120, South Korea

Keywords:
Sodium metal
Solid electrolyte
Redox-active electrolyte
Energy storage
Seawater battery

A B S T R A C T

Seawater batteries (SWBs), which utilize sodium ions instead of lithium ions, hold significant promise due to the abundance and cost-effectiveness of raw materials. Additionally, SWBs can achieve high theoretical capacities with Na metal anode, and the introduction of redox-active electrolytes enhances the reversibility during Na metal plating and stripping. However, under certain conditions, such as high current density and extended distance between the solid electrolyte and current collector, the redox-active electrolyte can result in inferior cycling performance due to issues with Na metal plating on the solid electrolyte surface. In this study, we investigated the mechanism of Na metal deposition on solid electrolyte surfaces using redox-active electrolytes owning electronic conductivity. Through electrochemical analyses, we elucidated the factors that influence Na metal plating: electronic conductivity, distance, and current density. By controlling the concentration and electronic conductivity of redox-active electrolytes, we established operational parameters to mitigate solid electrolyte cracking and ensure stable cycling, even under conditions of long distance and high current density. Given that instances of Na metal plating on solid electrolytes in battery systems are rarely reported, our research provides new insights and suggests innovative approaches to understanding the mechanisms of Na metal plating and cracking in solid electrolytes.

1. Introduction

With the advent of the Battery of Things (BOT) era, numerous electronic devices have transitioned from relying on dangling electric wires to enabling wireless charging and usage [1,2]. The market for Electric Vehicles (EVs) and Energy Storage Systems (ESS) is expected to steadily expand, leading to an explosive increase in demand for lithium-ion batteries (LIBs) [3]. However, the limited reserves of lithium resources on Earth and the volatility of raw material prices have highlighted the need for next-generation batteries that can serve as alternatives [4–6]. Seawater batteries (SWBs), which utilize sodium ions instead of lithium ions, have garnered significant attention due to their low raw material costs, material availability, and high safety [7,8]. Particularly, the abundant sodium ions in the cathode enable SWBs to achieve a high theoretical energy density (3051 Wh L^{-1}) [9].

To utilize seawater as a cathode material, the cell structure of SWBs consists of: (1) a cathode composed of carbon electrodes and Ti mesh submerged in seawater to facilitate OER/ORR reactions, (2) an anode composed of active materials, liquid electrolytes, and current collectors capable of stably storing sodium ions, and (3) a solid electrolyte such as Na Super Ion Conductor (NASICON) ceramic to prevent physical/electrical contact between the seawater and the anode [10]. Since the seawater cathode is abundant and operates as an open system, only the closed volume of the anode and solid electrolyte is considered in the energy density calculation for SWBs. The anode material thus determines the total cell capacity, and current research strategies on SWBs

* Corresponding authors.
E-mail addresses: stefano.passerini@kit.edu (S. Passerini), yikim@gachon.ac.kr (Y. Kim).
[1] These authors contributed equally to this work.

aim to increase volumetric capacity by utilizing high-energy-density anode materials and providing more space to store sodium ions [10–12].

The anodes of SWBs are quite similar to that of sodium-based battery systems, thus many kinds of anode materials and electrolytes have been implemented throughout their development (Table S1) [13–18]. Among these, Na metal has been extensively studied due to its high specific capacity (~1165 mAh g^{-1}) and low reduction potential (-2.71 V vs. SHE), which enables high energy density [19]. Previous studies have reported that using a saturated Na-biphenyl + 1 M $NaPF_6$ in DME (NaBP) as a redox-active liquid electrolyte in SWBs can yield high areal capacity and enhance the reversibility of Na metal plating and stripping (Table S2) [20–22]. In the study of Y. Jung, NaBP facilitates the discharge of dead sodium due to its redox activity, thereby enhancing coulombic efficiency (CE). Additionally, it minimizes the continuous consumption of the liquid electrolytes that lead to the formation of the thick SEI layer including NaF and Na_2CO_3. However, under varying charge/discharge conditions, such as high current density for high power applications or long distances between NASICON and the current collector for high energy density, the use of redox-active electrolyte leads to low reversibility due to the cracking of the solid electrolyte. This fracture is believed to occur because the Na metal in contact with the NASICON applies mechanical stress to the solid electrolyte under harsh charging conditions [23].

We anticipate that the primary reason for the difference in reversibility according to the conditions is the electronic conductivity of the redox-active electrolytes. The correlation between electronic conductivity and the metal plating position has been reported in many papers [24]. Sang-Hong et al. reported that, when a 3D electrode structure was designed differently, metal plating first occurred at positions with high electronic conductivity [25]. This study demonstrates through simulations that layers with high electronic conductivity, which induce an increased metal reaction flux, are favoured for metal nucleation. Moreover, several studies have reported that metal plating is possible in the pores of solid electrolytes when internal electronic conductivity is present [26]. Therefore, when using a redox-active electrolyte, there is a possibility of metal deposition on the surface of the solid electrolyte, where electronic conductivity is abundant due to direct contact with the redox-active electrolyte. The metal plating locations can be divided into 1) the current collector surface, 2) the pores of the solid electrolyte, and 3) the surface of the solid electrolyte. While many papers have reported cases 1) and 2), it was difficult to find relevant studies reporting metal plating on the surface of solid electrolytes.

In this study, we analyse the mechanism of metal deposition on solid electrolyte surfaces using NaBP as redox-active electrolyte with electronic conductivity, identifying three influencing factors: electronic conductivity, distance between the solid electrolyte and the current collector, and current density. The electronic conductivity was adjusted by varying the biphenyl concentration in the electrolyte and measured by Isothermal Transient Ionic Current (ITIC) method. Each factor was analysed through electrochemical methods, including overpotential measurements and electrochemical impedance spectroscopy (EIS), as well as through additional designed quartz cell systems. Ultimately, we have defined application parameters that minimize NASICON cracking and ensure stable cycling under high current conditions, while leveraging the high reversibility afforded by the electronic conductivity of redox-active electrolytes.

2. Materials and methods

Preparation of electrolytes Biphenyl (99.5 %, Sigma-Aldrich) was added into the 1,2-Dimethoxyethane (99 %, Alfa Aesar) solvent, from which moisture was removed by molecular sieves to obtain a 2 M (0.1, 0.5, and 1 M) solution. After the solution was stirred for more than 1 h, a corresponding amount of Na metal was added to saturate the solution. After stirring for over 10 h, 1 M of Sodium hexafluorophosphate ($NaPF_6$, 98 %, Alfa Aesar) salts and an additional 0.5 M of Na metal were added to the solution for oversaturation. After being stirred for 2 h, the solutions were completely prepared and referred to as saturated sodium-2 M (0.1 M, 0.5 M, and 1 M) biphenyl in dimethoxyethane (n M NaBP). All preparation steps were conducted in an Ar-filled glove box with H_2O and O_2 content of less than 1 ppm.

Electrochemical measurements Electrochemical tests such as galvanostatic cycling and EIS were conducted using 2465-type seawater battery coin cells. NASICON solid electrolyte (obtained from 4TO ONE Energy) was attached at the cap, and the 1, 2, and 4 mm gap between NASICON and the current collector was fixed by welding a stainless-steel (SUS) spacer and SUS304 mesh without using a spring. The electrolyte filled the whole volume of the cell without using a separator. The cathode material used was natural seawater with the addition of 0.4 M sodium ferrocyanide to maintain pH stability and a carbon felt (6 cm × 4 cm) as the cathode current collector. Galvanostatic cycling was performed using a WonATech WBCS 3000 battery tester. EIS was conducted using Biologic VSP-300 in the range of 7 MHz to 1 Hz (10 mV amplitude). The total conductivity was measured by the ITIC method, which used two SUS electrodes with a 2~2.5 cm Teflon tube. The ionic currents were measured at 0.1 V for 1 h by a Biologic VSP-300 potentiostat.

Material characterization The surfaces of plated Na metal on NASICON, glass fiber separator, and stainless-steel current collector were investigated by an SEM and EDS instrument (Quanta 200FEGinstrument). A quartz-type cell that has diameter of 12 π was assembled and Na metal plated on the SUS mesh was rinsed by DME before SEM and EDS analysis. The viscosity of NaBP was measured by a viscometer (Brookfield DV-1) in an Ar-fillied glove box at 21 °C.

3. Results and discussion

The anode part of the SWB is composed of a NASICON ($Na_{1+x}Zr_2Si_xP_{3-x}O_{12}$) solid electrolyte and a liquid electrolyte containing redox-active materials such as saturated Na-n M biphenyl + 1 M $NaPF_6$ in DME (NaBP), with an anode-free configuration to achieve high energy density (Figure S1a). The structure of SWBs, which separates the seawater and anode with NASICON, enables the use of redox-active electrolytes (anolytes) owning electronic conductivity. Given the structural configuration of the anode in SWBs, where NASICON and redox-active electrolytes are electronically connected, it is highly conceivable that Na metal plating can occur on the surface of NASICON or in its pores (Fig. 1a-c). Recent studies have shown that the growth of Na dendrites along grain boundaries into the internal pores of the solid electrolyte can lead to cracks, and the nonnegligible electronic conductivity in the pores of the solid electrolyte also influences the position of Na metal deposition [27]. Although metal nucleation in the pores of solid electrolytes has been reported, it remains challenging to determine whether the plated metal is on the surface of the solid electrolyte or the current collector, even in all-solid-state battery systems.

Accurately determining the initial location of Na metal plating is crucial within the SWBs. To identify this, a quartz cell that NASICON adhered to inside a quartz tube was designed to separate the anode and cathode (Figure S1b). Using a transparent quartz cell allows for the direct observation of Na metal formation at the interface between the current collectors and the solid electrolytes. When the 1 M $NaPF_6$ in DME electrolyte is used in the quartz cell, Na dendrites grow and crack the NASICON, resulting in gas evolution from the cathode side due to direct contact with external seawater, as shown in Fig. 1d. However, it was difficult to visually confirm the position of metal plating in the opaque, dark-green NaBP (Fig. 1e).

After washing the quartz cell with plated Na metal through a 1 mA cm^{-2} current density during 5 h of charging, differences in morphology were observed when using redox-active and conventional electrolytes, as shown in Fig. 1f–i. In Fig. 1f and g, only 1-2 small, dark point-like cracks were observed on the surface of NASICON with conventional electrolytes. In contrast, plated Na metal was uniformly distributed across the surface of NASICON when using a redox-active electrolyte, as

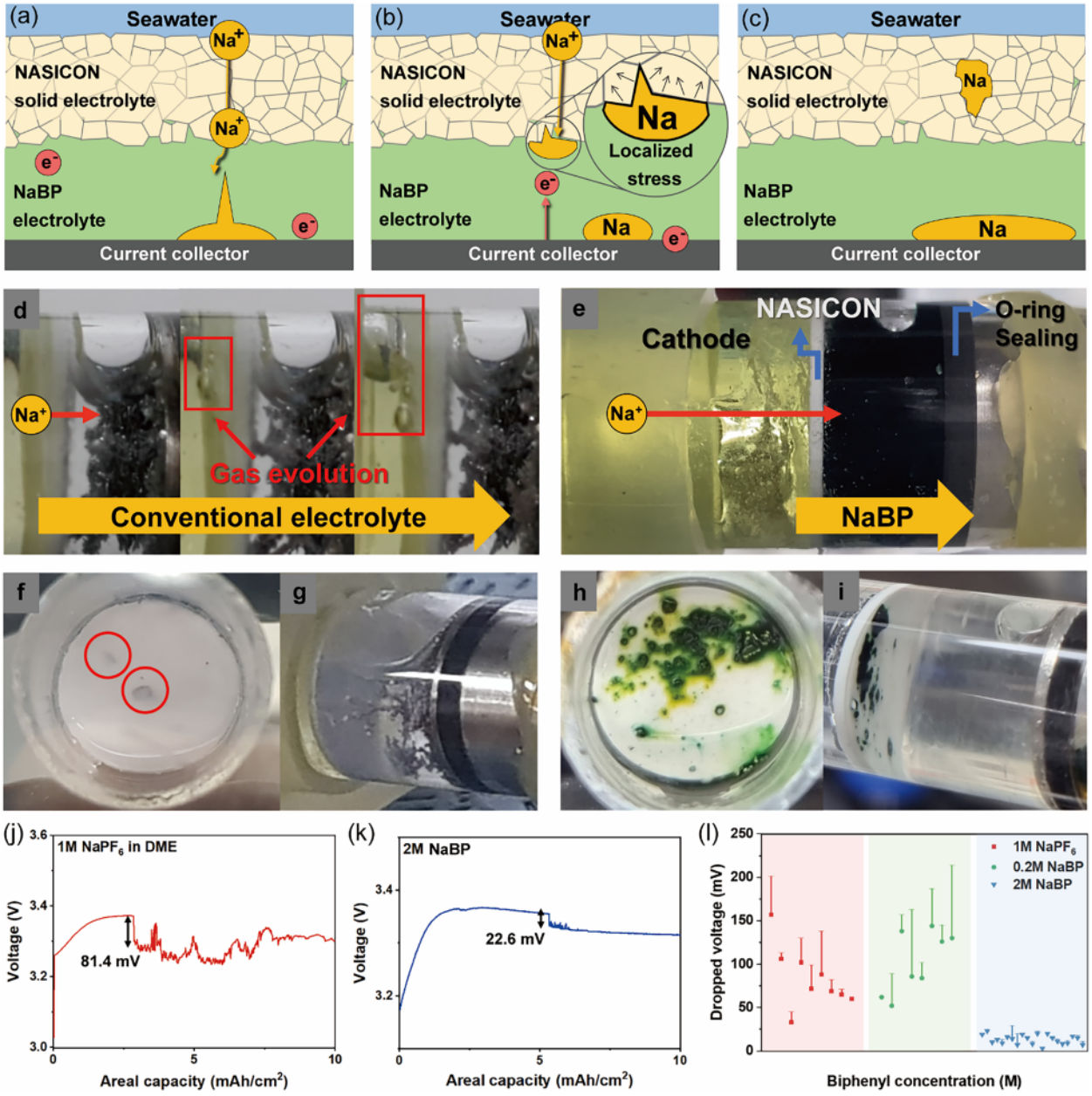

Fig. 1. Scheme of possible metal plating positions in an SWB full cell: (a) current collector side plating, (b) NASICON surface plating, and (c) pores of NASICON plating. Quartz cell structure for SWB full cell during sodiation with different electrolytes; (d) 1 M $NaPF_6$ in DME, (e) 2 M NaBP. Quartz cell washing with DME solvent after 4 mAh cm^{-2} Na metal plating with different electrolytes, (f-g) 1 M $NaPF_6$ in DME, (h-i) 2 M NaBP. Dropped voltage measurements with different electrolytes, (j) 1 M $NaPF_6$ in DME, (k) 2 M NaBP, and (l) repeated measurements of dropped voltage with various trials.

shown in Fig. 1h and i.

Furthermore, differences between conventional and redox-active electrolytes were also identified through voltage profiles. When using conventional electrolytes, a substantial voltage drop of about 80 mV occurred, with notable fluctuations following the initial drop, indicating unstable charging (Fig. 1j). However, when using a redox-active electrolyte, a voltage drop of only about 22 mV was observed due to short circuits driven by cracks, with no significant fluctuations thereafter (Fig. 1k). This phenomenon was consistently observed in multiple trials, as shown in Fig. 1l, varying with the concentration of biphenyl.

For neat 1 M $NaPF_6$ (i.e., without biphenyl additive) and 0.2 M NaBP electrolytes, the range of voltage drops due to cracks was between 50–150 mV, frequently exceeding 200 mV at the lowest point after the initial drop (Figure S2a). However, when using 2 M NaBP electrolyte, even with the occurrence of cracks, the voltage drop mostly remained below 30 mV, with the lowest point around 50 mV (Figure S2b). These phenomena are expected to vary with the concentration of biphenyl, which affects the plating position of Na metal and consequently the morphology of cracks.

Preliminary experiments have demonstrated that the concentration of biphenyl can influence both the position of Na metal plating and the voltage profiles due to short circuits. It has been documented that polycyclic aromatic hydrocarbons (PAHs), such as biphenyl, dissolved together with Na metal in a solvent can act as redox-active materials [28]. There is an interaction between PAHs and alkali metals that involves charge transfer, where the alkali metal donates electrons to the PAHs, occupying the previously unoccupied π^* orbitals [11,29]. In this scenario, they consist of Na^+ cations and biphenyl anions, generating delocalized electrons that contribute significantly to the electronic conductivity, a pivotal characteristic affecting the positions for metal

plating. Therefore, the increase of the biphenyl's concentration results in the rise of the redox-active electrolyte's electronic conductivity. The ITIC method was utilized to separately evaluate the ionic and electronic conductivities of the redox-active electrolyte, as illustrated in Fig. 2 [30]. A measurement cell was constructed by sealing coin cell caps (with stainless steel serving as a current collector) on both ends of a 25 mm long PTFE tube with a diameter of 19 mm, as depicted in Fig. 2a. The ITIC method involves applying a constant voltage while measuring current density. The initial current density curve is linked to the mobility of ions within the electrolytes, contributing to ionic conductivity, whereas the subsequent constant current density is associated with electronic conductivity within the electrolyte, as depicted in Fig. 2b. Through fitting and analysing these curves, it is feasible to separate and evaluate both the ionic and electronic conductivity using the formula:

$$J(t) = \sigma_{dc,e}\ U/L + \left(\sigma_{dc,Na^+} U/L\right)\exp\left\{\left(\quad \mu_{Na^+} U/L^2\right)t\right\} \tag{1}$$

Here J denotes the current density, L the distance between the two electrodes, μ_{Na^+} the sodium ion mobility, $\sigma_{dc,e}$ and σ_{dc,Na^+} the electronic and ionic conductivities, respectively, t the time, and U the voltage between the two electrodes.

To maintain the minimum ionic conductivity required for ion transport in 0.1 M to 2 M biphenyl, 1 M $NaPF_6$ was added as the supporting electrolyte. Consequently, variations in solubility and viscosity may lead to differences in chemical pre-sodiation. Therefore, discharge tests were conducted to quantify the amount of dissolved Na, as depicted in Fig. 2c and Figures S3a-b. The SWB coin cells, which contains 150 μL of NaBP, a glass fiber (GF/A, Whatman) separator, and a SUS current collector, was discharged with a current of 0.25 mA cm^{-2}. The concentrations of biphenyl and Na increased proportionally up to 0.5 M, but the rate of increase in Na concentrations noticeably decreased from 0.5 M to 2 M biphenyl. As shown in Fig. 2d, the electronic conductivity increased from 1.65 mS cm^{-1} at 0.1 M to 4.24 mS cm^{-1} at 2 M NaBP, correspondingly with the Na concentration ratio. This rise is attributed to the increased electronic conductivity resulting from the formation of biphenyl anions as Na metal forms Na cations and biphenyl anions. In contrast, the ionic conductivity reached its highest value of 2.55 mS cm^{-1} at 0.5 M, compared to 1.45 at 0.1 M and 0.89 mS cm^{-1} at 2 M. This decrease in ionic conductivity at higher NaBP concentrations is expected due to the rise in viscosity caused by the increasing biphenyl concentration (Figure S3c). Additionally, the conductivity of 0.5 M NaBP was measured across temperatures ranging from 0 °C to 40 °C by ITIC method, considering the temperature of seawater (Figure S4a, b) [31]. The electronic conductivity displayed an increasing trend with temperature, while the ionic conductivity peaked at 30 °C, reaching a maximum value of 3.381 mS cm^{-1}.

The strategy for enhancing the energy density of seawater batteries involves increasing the volume of the anode to enlarge the proportion of active material. It is crucial to widen the gap between the current collector and NASICON and then plate the Na metal, as illustrated in Fig. 3a and 3b [10,12]. However, widening the distance resulted in the occurrence of NASICON cracks due to Na metal, consequently preventing a proportional increase in the energy density, as the instances shown in Figure S2. Generally, dendrite formation and solid electrolyte fracture are closely linked to both electronic and ionic conductivities in metal anode systems [32]. According to Sand's time equation, when the current density is high and ionic conductivity is insufficient, the ion concentration on the electrode surface decreases, accelerating the initial rate of dendrite formation [33,34]. Additionally, in all-solid-state

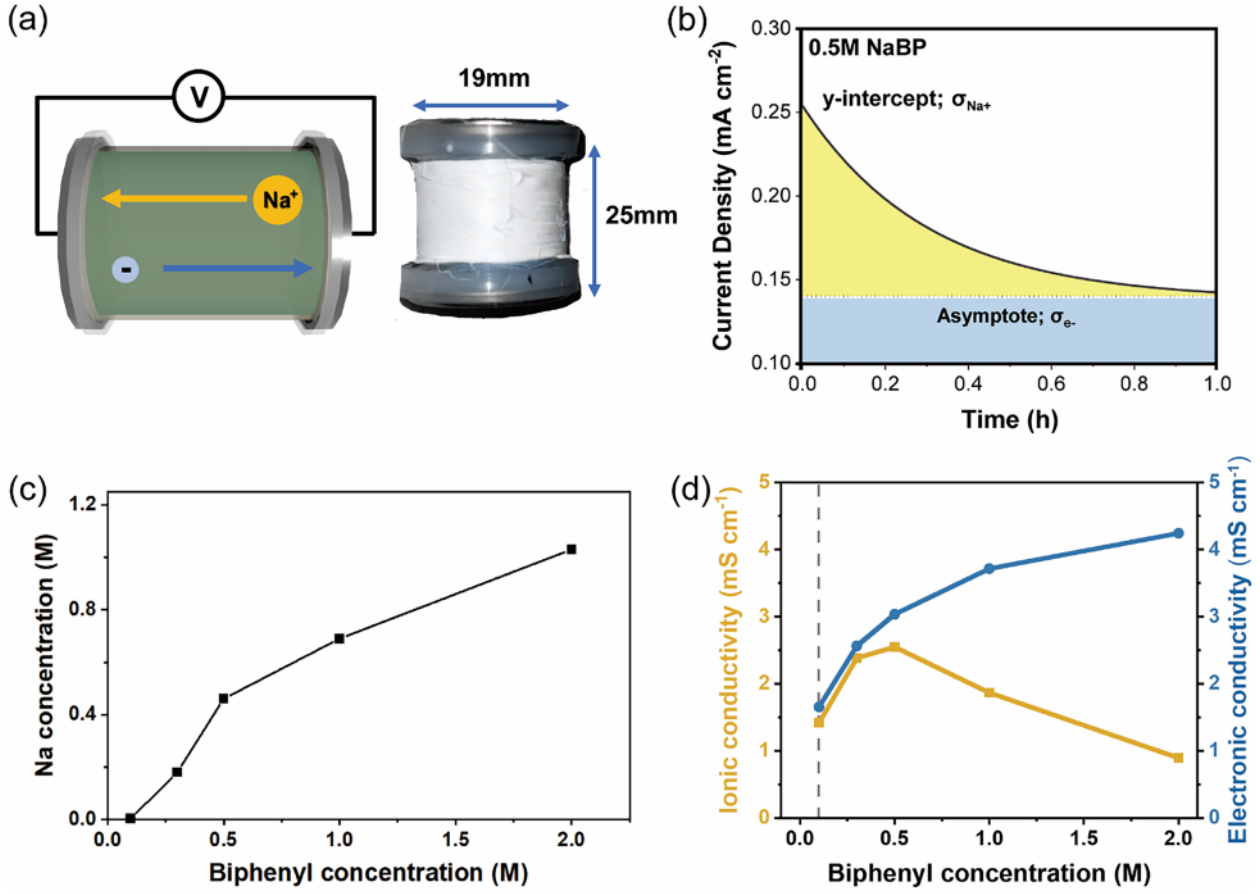

Fig. 2. Isothermal transient ionic current (ITIC) method for measuring ionic and electronic conductivity. (a) Schematic and actual image of the cell used for ITIC measurement. (b) Graph showing measured ITIC current density vs. time for 0.5 M NaBP electrolyte. (c) Relationship between measured Na concentration and biphenyl concentration during the 1st discharge capacity. (d) Measured ionic and electronic conductivity of the electrolytes with varying biphenyl concentrations.

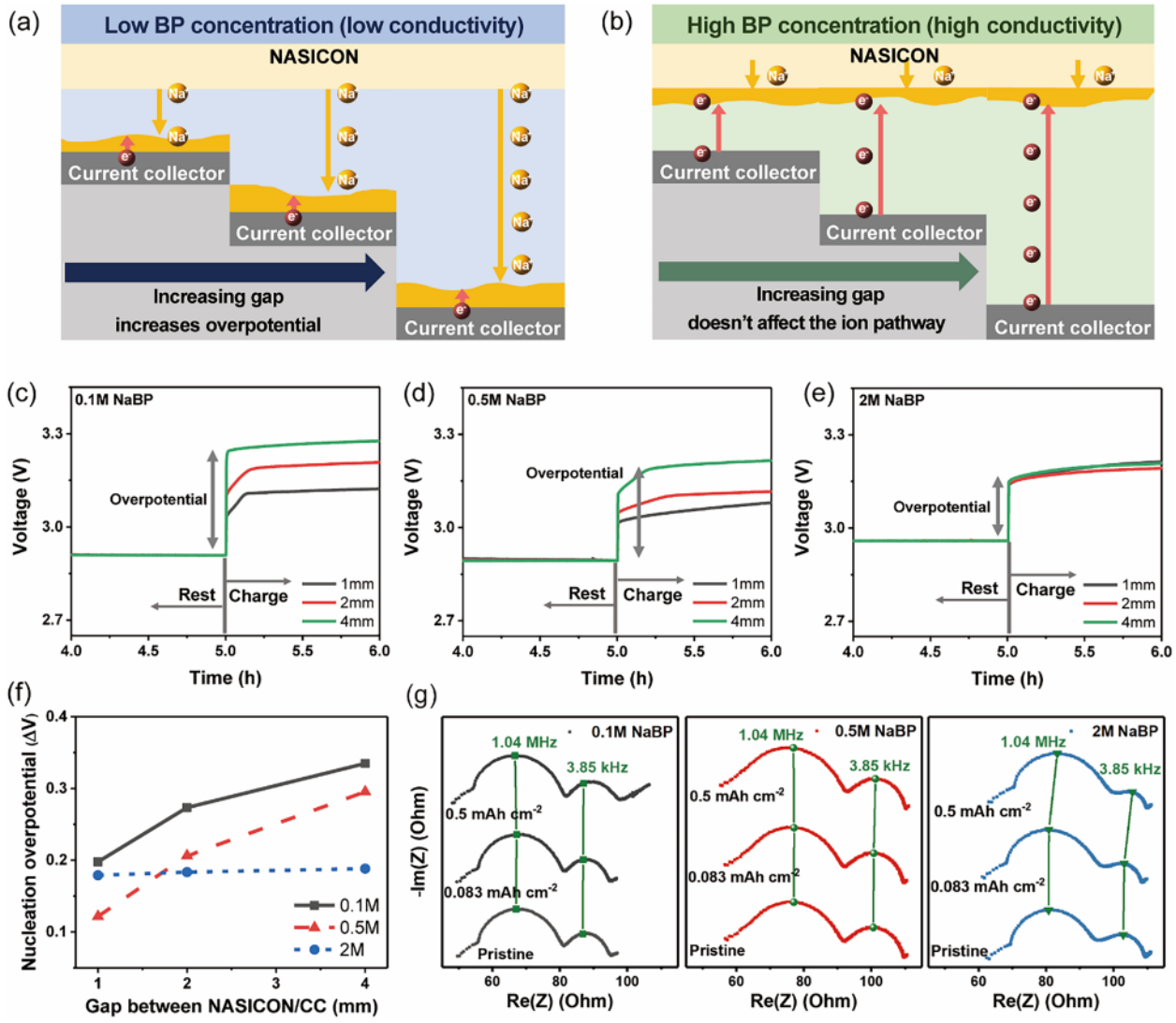

Fig. 3. Illustrations depicting the increasing gap between the solid electrolyte and the current collector with the Na^+ ion transport pathway at (a) low biphenyl concentration with low conductivity and (b) high biphenyl concentration with high conductivity. Voltage profiles of initial nucleation with different electrolytes: (c) Sat.Na-0.1 M biphenyl + 1 M $NaPF_6$ in DME, (d) Sat.Na-0.5 M biphenyl + 1 M $NaPF_6$ in DME, and (e) Sat.Na-2 M biphenyl + 1 M $NaPF_6$ in DME. (f) Nucleation overpotential versus gap between NASICON and current collector. (g) Electrochemical impedance spectroscopy (EIS) measurements for different biphenyl concentrations compared to 1 mAh cm^{-2} metal plating.

batteries, the negligibly high electronic conductivity of the solid electrolyte can induce the formation of metal dendrites in the solid electrolyte [35]. This suggests that focusing on reducing the electronic conductivity rather than improving the ionic conductivity is necessary in some cases. Conversely, there are strategies for uniformly increasing the electronic conductivity of the current collector to lower the nucleation overpotential [36]. Therefore, proper adjustment of both the electronic and ionic conductivities is crucial for preventing solid electrolyte damage caused by Na metal dendrites, thereby enhancing battery cyclability. Hence, the distance factors were examined at three different values (1 mm, 2 mm, and 4 mm, Figure S5a, b) in a coin cell structure with three concentrations of biphenyl (0.1 M, 0.5 M, and 2 M) to investigate the correlation between the distance and the ionic/electronic conductivity of the electrolyte by the metal plating mechanism. As the gap between the current collector and NASICON increases, the distance of the space that the liquid electrolyte occupies also expands along with the pathway for Na^+ ion transportation, which affects the resistance of the anolyte (Fig. 3a) according to

$$R = l/\sigma A, \tag{2}$$

where R denotes the resistance, l denotes the distance, σ denotes the conductivity, and A denotes the area.

According to Formula (2), the electrolyte resistance (R) increases as the electrolyte distance (l) increases, leading to a higher Ohmic overpotential during the charging process of the Na metal [37]. At lower concentrations of NaBP (0.1 M and 0.5 M), increases in charging voltage were observed with a wider gap between the NASICON and the current collector consistent with expectations, indicating a higher Ohmic overpotential (Fig. 3a, 3c, and 3d). However, there was no significant rise in the overpotential despite the widening distance when using a 2 M NaBP electrolyte, as illustrated in Fig. 3e. This observation deviates from cases where Na metal plating occurs on the current collector, leading to an expected shift in the metal plating position on the NASICON surface, as evidenced by previous cell disassembly.

In the case where Na metal is plated on the NASICON surface as shown in Fig. 3b, Na^+ ions do not utilize the pathway provided by the liquid electrolyte. Consequently, the increased distance minimally affects Na metal plating on the NASICON surface, resulting in a similar Ohmic overpotential. Furthermore, it was observed that the charging overpotential increased when the biphenyl concentration was below 0.5

M, as depicted in Fig. 3f. For NaBP at a concentration of 0.1 M, which has similar ionic conductivity to that of 2 M NaBP, the charging voltage increased with the electrolyte distance, suggesting that differences in the electronic conductivity of the electrolyte drive this phenomenon. These distinct electrochemical phenomena between low biphenyl concentrations and 2 M biphenyl were further validated through electrochemical impedance spectroscopy (EIS).

Prior research has highlighted changes in grain boundary resistance observed via EIS analysis when metal penetration occurs in solid-state electrolytes [38,39] In the coin cell structure with a 4 mm gap, EIS was compared between the pristine state and post-charging after reaching a current density of 1 mA cm ^{2} (Fig. 3g). The first semicircle, with a frequency of 1.04 MHz, primarily reflects the resistance element at the grain boundary of NASICON solid electrolytes [11]. For 0.1 M and 0.5 M NaBP, negligible changes in resistance were observed in the first semicircle when Na metal was charged to 0.5 mAh cm ^{2}, indicating that at low concentrations of NaBP, substantial changes do not occur on the NASICON surface during Na metal charging. In contrast, at a 2 M NaBP concentration, there was a significant increase in the resistance of the first semicircle, likely attributed to Na metal formation at the grain boundaries of the NASICON surface, consistent with other studies [38, 39].

The second semicircle, with a frequency of 3.85 kHz, primarily reflects charge transfer resistance [11]. During the charging process, minimal changes in the size of the second semicircle were observed for low concentrations of NaBP (0.1 M, 0.5 M). However, with 2 M NaBP, a reduction in the size of the second semicircle was noted, suggesting a decrease in charge transfer resistance due to Na metal formation on the NASICON surface, reducing the impact of NaBP on charge transfer at the NASICON interface. These results imply that charge transfer reactions predominantly occur on the NASICON surface at a 2 M concentration of NaBP.

While previous electrochemical analyses implicitly suggested that Na metal could be deposited on the NASICON surface when using a high-concentration biphenyl electrolyte, a more precise understanding is necessary. To address this, a metal plating experiment was conducted in a quartz cell with a 1cm gap filled with GF/A, as depicted in Figure S6a. Upon disassembling the cell after charging, it was challenging to observe any traces of Na metal on the NASICON surface and the glass fiber separator on the NASICON side with the 0.5 M biphenyl electrolyte. However, pieces of Na metal were visible on the current collector and the separator of the current collector side, as shown in Figure S6b. Conversely, it was difficult to detect any Na metal on the current collector side of a quartz cell prepared under the same conditions, but using a 2 M biphenyl electrolyte; instead, most of the Na metal was found on the NASICON side (Figure S6c).

Subsequent SEM and EDS analyses of the NASICON surface revealed no traces of Na metal when using the 0.5 M NaBP electrolyte (Fig. 4a-f). However, when plating Na metal using a 2 M NaBP electrolyte, plated Na metal on the NASICON surface was observed (Fig. 4g-l). Confirmation through EDS showed significantly higher counts of Na K elements compared to the NASICON itself, indicating the presence of Na metal. Additionally, the absence of Si K and P K components further implied the presence of Na metal. Thus, although directly confirming the location of plated Na metal in situ with an opaque redox-active electrolyte was challenging, post-analysis after cell separation provided direct confirmation that Na metal could plate on the NASICON surface.

Although prior experiments confirmed the plating of metal on the NASICON surface, additional research was conducted to assess its impact on cyclability. The plating of Na metal on the NASICON surface hinders the prolonged use of thick anodes and causes NASICON cracking due to localized stress, as depicted in Fig. 5a. Therefore, despite the benefits of a high CE from the redox-active electrolyte, a decrease in cycle performance is evident. Conversely, reducing the redox-active material content results in issues with low CE due to the formation of useless dead Na and SEI layers, illustrated with the 1 M $NaPF_6$ electrolyte in Fig. 5b.

The cycle life of 0 M, 0.5 M, and 1 M NaBP electrolytes in SWB coin cells was evaluated under extreme conditions with a 4 mm gap anode and a current density of 2.6 mA cm ^{2}. Specifically, it was noted that the 0 M biphenyl + 1 M $NaPF_6$ in DME electrolyte initially demonstrated low CE as anticipated (Figure S7a). After approximately 50 cycles, the development of a sufficient SEI layer and dead Na formation led to higher CE, yet subsequent dendrite formation caused NASICON

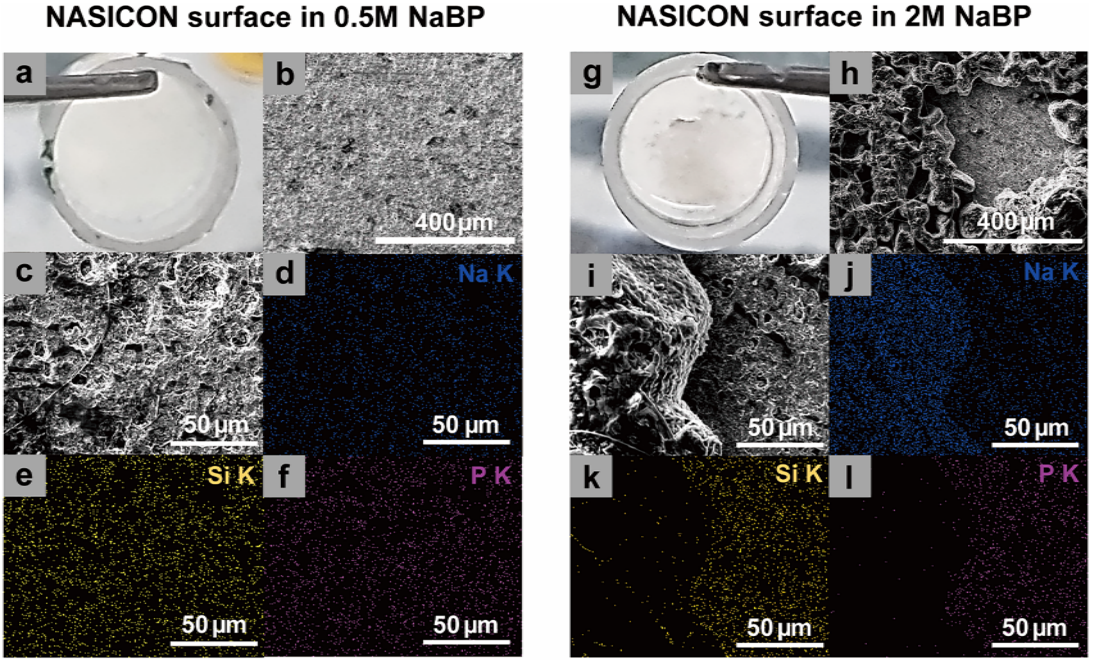

Fig. 4. Observation of disassembled NASICON after 5 mAh cm^{-2} Na metal plating with different electrolytes; Sat.Na-0.5 M BP + 1 M $NaPF_6$ in DME and Sat.Na-2 M BP + 1 M $NaPF_6$ in DME. (a, g) Real image of disassembled NASICON surface with quartz cell structure. (b, h) SEM images of NASICON surface at 200x magnification, (c, i) 1000x magnification, and EDS images of (d, j) Na K element, (e, k) Si K element, and (f, l) P K element.

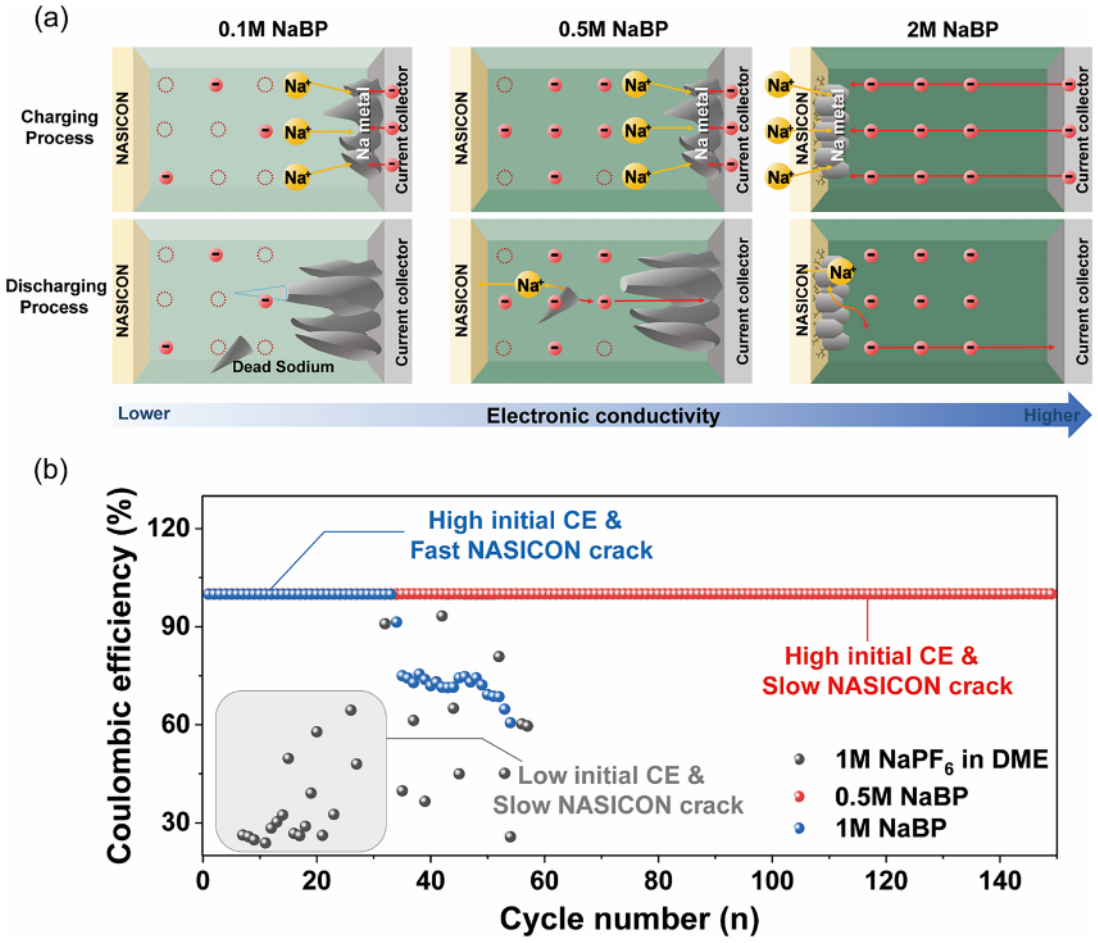

Fig. 5. (a) Scheme illustrating the trade-off with varying biphenyl concentrations in SWB anode parts. (b) Relationship between cycle number and coulombic efficiency across different biphenyl concentrations.

cracking, resulting in cell failure. For the 2 M NaBP electrolyte, unstable voltage profiles were observed during the charging process of the first cycle under the conditions of the 4 mm gap and high current density, rendering cycle confirmation impossible (Figure S7b). In contrast, the initial high CE characteristic of redox-active electrolytes was noted with a lower concentration of 1 M NaBP (Figure S7c). However, cell operation was halted due to the impact of Na metal plating on the NASICON surface, leading to cracks and short circuits. In the case of 0.3 M NaBP, high CE was maintained for more than 70 cycles initially. However, because of its relatively low conductivity, it exhibited low voltage efficiency, and a decrease in CE was observed after the 80th cycle (Figure S7d, e). Consequently, the advantages of high CE and cyclability from the current collector due to metal were demonstrated through the cell operation to 500 cycles at an intermediate concentration point of 0.5 M NaBP (Figure S7f, g).

4. Conclusion

A key approach to enhancing energy density in SWBs involves increasing the anode volume, which in turn widens the distance between the solid electrolyte and the current collector. However, when employing a redox-active electrolyte that improves the reversibility of Na metal plating/stripping, NASICON cracking occurs more rapidly than anticipated. This is presumed to be due to the high electronic conductivity of the concentrated NaBP redox-active electrolyte, leading to the assumption that Na metal plating occurs on the NASICON surface rather than on the current collector.

To investigate this phenomenon of accelerated NASICON cracking, we conducted experiments involving quartz cell test, nucleation overpotential, and EIS analyses to identify the trend of Na metal plating with a high concentration of NaBP redox-active material, which differed from that observed in conventional electrolytes where plating typically occurs from the current collector. Furthermore, SWB coin cell disassembly and SEM-EDS analysis were employed to examine the morphology of Na metal plated on the surface of NASICON.

Ultimately, our results indicated that reducing the concentration of redox-active material led to an initial CE issue due to dead Na formation during the Na metal plating/stripping process. Conversely, increasing the concentration led to difficulties in utilizing the internal volume of the anode due to metal formation on the NASICON surface. Therefore, there exist upper and lower limits to the concentration of redox-active material, depending on cell conditions such as distance and current density. This analysis is significant as it provides an approach for achieving more stable operation of redox-active electrolytes previously used with Na metal in SWBs. Considering the rarity of metal plating on solid electrolyte surfaces in battery systems, our research offers valuable insights and suggests novel approaches for comprehending the mechanisms of metal plating and cracking in solid electrolytes.

CRediT authorship contribution statement

Seyoung Lee: Writing – review & editing, Writing – original draft, Visualization, Investigation, Formal analysis, Data curation, Conceptualization. **Youngjae Jung:** Writing – review & editing, Writing – original draft, Visualization, Methodology, Investigation, Data curation, Conceptualization. **Jihun Cho:** Methodology, Investigation, Data

curation. **Dowan Kim:** Writing – review & editing, Validation. **Hyeonseok Lee:** Writing – review & editing, Investigation. **Seohae Kim:** Visualization, Validation. **Hyo Jin:** Validation, Formal analysis. **Hyeji Min:** Validation, Investigation. **Wang-Geun Lee:** Writing – review & editing, Funding acquisition. **Youngsik Kim:** Supervision, Project administration, Conceptualization. **Stefano Passerini:** Writing – review & editing, Supervision. **Yongil Kim:** Writing – review & editing, Supervision, Conceptualization.

Declaration of competing interest

The authors declare that they have no known competing financial interests or personal relationships that could have appeared to influence the work reported in this paper.

Data availability

Data will be made available on request.

Acknowledgement

This work was supported by the Technology Development Program (00273382) funded by the Ministry of SMEs and Startups (MSS, Korea). S.P. acknowledges the support of the Helmholtz Association.

References

[1] M. Waseem, M. Ahmad, A. Parveen, M. Suhaib, Battery technologies and functionality of battery management system for EVs: current status, key challenges, and future prospectives, J. Power Sources 580 (2023) 233349, https://doi.org/10.1016/j.jpowsour.2023.233349.
[2] M. Fichtner, K. Edström, E. Ayerbe, M. Berecibar, A. Bhowmik, I.E. Castelli, S. Clark, R. Dominko, M. Erakca, A.A. Franco, A. Grimaud, B. Horstmann, A. Latz, H. Lorrmann, M. Meeus, R. Narayan, F. Pammer, J. Ruhland, H. Stein, T. Vegge, M. Weil, Rechargeable batteries of the future—The state of the art from a BATTERY 2030+ perspective, Adv. Energy Mater. 12 (2022) 2102904, https://doi.org/10.1002/aenm.202102904.
[3] F. Degen, M. Winter, D. Bendig, J. Tübke, Energy consumption of current and future production of lithium-ion and post lithium-ion battery cells, Nat. Energy 8 (2023) 1284–1295, https://doi.org/10.1038/s41560-023-01355-z.
[4] G. Song, H. Bin Son, D.-Y. Han, M. Je, S. Nam, S. Park, A renewable future: a comprehensive perspective from materials to systems for next-generation batteries, Mater. Chem. Front. 5 (2021) 3344–3377, https://doi.org/10.1039/D1QM00071C.
[5] C.P. Grey, D.S. Hall, Prospects for lithium-ion batteries and beyond—a 2030 vision, Nat. Commun. 11 (2020) 6279, https://doi.org/10.1038/s41467-020-19991-4.
[6] J.T. Frith, M.J. Lacey, U. Ulissi, A non-academic perspective on the future of lithium-based batteries, Nat. Commun. 14 (2023) 420, https://doi.org/10.1038/s41467-023-35933-2.
[7] S.T. Senthilkumar, W. Go, J. Han, L. Pham Thi Thuy, K. Kishor, Y. Kim, Y. Kim, Emergence of rechargeable seawater batteries, J. Mater. Chem. A 7 (2019) 22803–22825, https://doi.org/10.1039/C9TA08321A.
[8] S.M. Hwang, J.-S. Park, Y. Kim, W. Go, J. Han, Y. Kim, Y. Kim, Rechargeable seawater batteries—from concept to applications, Adv. Mater. 31 (2019) 1804936, https://doi.org/10.1002/adma.201804936.
[9] D.H. Kim, H. Choi, D.Y. Hwang, J. Park, K.S. Kim, S. Ahn, Y. Kim, S.K. Kwak, Y.-J. Yu, S.J. Kang, Reliable seawater battery anode: controlled sodium nucleation via deactivation of the current collector surface, J. Mater. Chem. 6 (2018) 19672–19680, https://doi.org/10.1039/C8TA07610C.
[10] Y. Kim, K. Shin, Y. Jung, W.-G. Lee, Y. Kim, Development of Prismatic Cells for Rechargeable Seawater Batteries, Adv. Sustain. Syst. 6 (2022) 2100484, https://doi.org/10.1002/adsu.202100484.
[11] Y. Kim, A. Varzi, A. Mariani, G.-T. Kim, Y. Kim, S. Passerini, Redox-mediated red-phosphorous semi-liquid anode enabling metal-free rechargeable Na-seawater batteries with high energy density, Adv. Energy Mater. 11 (2021) 2102061, https://doi.org/10.1002/aenm.202102061.
[12] Y. Jung, S. Lee, D. Kim, H. Lee, S. Kim, J. Cho, H. Jin, Y. Kim, J.-S. Park, W.-G. Lee, Vertically arranged electrode structures with high energy density for seawater batteries, J. Power Sources 592 (2024) 233960, https://doi.org/10.1016/j.jpowsour.2023.233960.
[13] H. Kim, J.-S. Park, S.H. Sahgong, S. Park, J.-K. Kim, Y. Kim, Metal-free hybrid seawater fuel cell with an ether-based electrolyte, J. Mater. Chem. A 2 (2014) 19584–19588, https://doi.org/10.1039/C4TA04937C.
[14] J.-K. Kim, F. Mueller, H. Kim, D. Bresser, J.-S. Park, D.-H. Lim, G.-T. Kim, S. Passerini, Y. Kim, Rechargeable hybrid sea water fuel cell, NPG Asia Mater. 6 (2014) e144, https://doi.org/10.1038/am.2014.106.
[15] Z.W. Seh, J. Sun, Y. Sun, Y. Cui, A highly reversible room-temperature sodium metal anode, ACS Cent. Sci. 1 (2015) 449–455, https://doi.org/10.1021/acscentsci.5b00328.
[16] S.M. Hwang, J. Kim, Y. Kim, Y. Kim, Na-Ion storage performance of amorphous Sb_2S_3 nanoparticles: anode for Na-Ion batteries and seawater flow batteries, J. Mater. Chem. A 4 (2016) 17946–17951, https://doi.org/10.1039/C6TA07838A.
[17] J.-K. Kim, F. Mueller, H. Kim, S. Jeong, J.-S. Park, S. Passerini, Y. Kim, Eco-friendly energy storage system: seawater and ionic liquid electrolyte, ChemSusChem 9 (2016) 42–49, https://doi.org/10.1002/cssc.201501328.
[18] Y. Kim, J.-K. Kim, C. Vaalma, G.H. Bae, G.-T. Kim, S. Passerini, Y. Kim, Optimized hard carbon derived from starch for rechargeable seawater batteries, Carbon 129 (2018) 564–571, https://doi.org/10.1016/j.carbon.2017.12.059.
[19] Y. Zhao, K.R. Adair, X. Sun, Recent developments and insights into the understanding of Na metal anodes for Na-metal batteries, Energy Environ. Sci. 11 (2018) 2673–2695, https://doi.org/10.1039/C8EE01373J.
[20] S. Lee, I.Y. Cho, D. Kim, N.K. Park, J. Park, Y. Kim, S.J. Kang, Y. Kim, S.Y. Hong, Redox-active functional electrolyte for high-performance seawater batteries, ChemSusChem 13 (2020) 2220–2224, https://doi.org/10.1002/cssc.201903564.
[21] Y. Kim, J. Jung, H. Yu, G.-T. Kim, D. Jeong, D. Bresser, S.J. Kang, Y. Kim, S. Passerini, Sodium biphenyl as anolyte for sodium–seawater batteries, Adv. Funct. Mater. 30 (2020) 2001249, https://doi.org/10.1002/adfm.202001249.
[22] Y. Jung, S. Lee, D. Kim, J. Park, S.J. Kang, Y. Kim, J.-S. Park, W.-G. Lee, Reversible Na plating/stripping with high areal capacity using an electroconductive liquid electrolyte system, ACS Appl. Mater. 15 (2023) 43656–43666, https://doi.org/10.1021/acsami.3c06554.
[23] Z. Ning, G. Li, D.L.R. Melvin, Y. Chen, J. Bu, D. Spencer-Jolly, J. Liu, B. Hu, X. Gao, J. Perera, C. Gong, S.D. Pu, S. Zhang, B. Liu, G.O. Hartley, A.J. Bodey, R.I. Todd, P. S. Grant, D.E.J. Armstrong, T.J. Marrow, C.W. Monroe, P.G. Bruce, Dendrite initiation and propagation in lithium metal solid-state batteries, Nature 618 (2023) 287–293, https://doi.org/10.1038/s41586-023-05970-4.
[24] S.T. Oyakhire, W. Zhang, A. Shin, R. Xu, D.T. Boyle, Z. Yu, Y. Ye, Y. Yang, J. A. Raiford, W. Huang, J.R. Schneider, Y. Cui, S.F. Bent, Electrical resistance of the current collector controls lithium morphology, Nat. Commun. 13 (2022) 3986, https://doi.org/10.1038/s41467-022-31507-w.
[25] S.-H. Hong, D.-H. Jung, J.-H. Kim, Y.-H. Lee, S.-J. Cho, S.H. Joo, H.-W. Lee, K.-S. Lee, S.-Y. Lee, Electrical conductivity gradient based on heterofibrous scaffolds for stable lithium-metal batteries, Adv. Funct. Mater. 30 (2020) 1908868, https://doi.org/10.1002/adfm.201908868.
[26] J. Zhao, Y. Tang, Q. Dai, C. Du, Y. Zhang, D. Xue, T. Chen, J. Chen, B. Wang, J. Yao, N. Zhao, Y. Li, S. Xia, X. Guo, S.J. Harris, L. Zhang, S. Zhang, T. Zhu, J. Huang, In situ observation of Li deposition-induced cracking in garnet solid electrolytes, Energy Environ. Mater. 5 (2022) 524–532, https://doi.org/10.1002/eem2.12261.
[27] S. Lee, K.-s. Lee, S. Kim, K. Yoon, S. Han, M.H. Lee, Y. Ko, J.H. Noh, W. Kim, K. Kang, Design of a lithiophilic and electron-blocking interlayer for dendrite-free lithium-metal solid-state batteries, Sci. Adv. 8 (2022) eabq0153, https://doi.org/10.1126/sciadv.abq0153.
[28] G. Wang, B. Huang, D. Liu, D. Zheng, J. Harris, J. Xue, D. Qu, Exploring polycyclic aromatic hydrocarbons as an anolyte for nonaqueous redox flow batteries, J. Mater. Chem. A 6 (2018) 13286–13293, https://doi.org/10.1039/C8TA03221A.
[29] F. Pan, J. Yang, C. Jia, H. Li, Q. Wang, Biphenyl-lithium-TEGDME solution as anolyte for high energy density non-aqueous redox flow lithium battery, J. Energy Chem. 27 (2018) 1362–1368, https://doi.org/10.1016/j.jechem.2018.04.008.
[30] G. Frenning, M. Nilsson, J. Westlinder, G.A. Niklasson, M.S. Mattsson, Dielectric and Li transport properties of electron conducting and non-conducting sputtered amorphous Ta2O5 films, Electrochim. Acta 46 (2001) 2041–2046, https://doi.org/10.1016/S0013-4686(01)00412-1.
[31] Y. Lu, L. Yang, Y. Zhang, Q. Zhao, L. Sang, F. Ding, H. Xu, Influence of simulating deep-sea environmental factors on cathodic performance of seawater battery, J. Ocean. Limnol. 38 (2020) 334–341, https://doi.org/10.1007/s00343-019-9102-0.
[32] X. Zhang, A. Wang, X. Liu, J. Luo, Dendrites in lithium metal anodes: suppression, regulation, and elimination, Acc. Chem. Res. 52 (2019) 3223–3232, https://doi.org/10.1021/acs.accounts.9b00437.
[33] J.N. Chazalviel, Electrochemical aspects of the generation of ramified metallic electrodeposits, Phys. Rev. A 42 (1990) 7355–7367, https://doi.org/10.1103/PhysRevA.42.7355.
[34] E.R. Cooper, M. Li, I. Gentle, Q. Xia, R. Knibbe, A deeper understanding of metal nucleation and growth in rechargeable metal batteries through theory and experiment, Angew. Chem. Int. Ed. 62 (2023) e202309247, https://doi.org/10.1002/anie.202309247.
[35] F. Han, A.S. Westover, J. Yue, X. Fan, F. Wang, M. Chi, D.N. Leonard, N.J. Dudney, H. Wang, C. Wang, High electronic conductivity as the origin of lithium dendrite formation within solid electrolytes, Nat. Energy 4 (2019) 187–196, https://doi.org/10.1038/s41560-018-0312-z.
[36] S. Liu, X. Zhang, R. Li, L. Gao, J. Luo, Dendrite-free Li metal anode by lowering deposition interface energy with Cu99Zn alloy coating, Energy Storage Mater. 14 (2018) 143–148, https://doi.org/10.1016/j.ensm.2018.03.004.

[37] J. Wu, L. Yuan, W. Zhang, Z. Li, X. Xie, Y. Huang, Reducing the thickness of solid-state electrolyte membranes for high-energy lithium batteries, Energy Environ. Sci. 14 (2021) 12–36, https://doi.org/10.1039/D0EE02241A.
[38] R. Chen, C. Yao, Q. Yang, H. Pan, X. Yu, K. Zhang, H. Li, Enhancing the thermal stability of NASICON solid electrolyte pellets against metallic lithium by defect modification, ACS Appl. Mater. Interfaces 13 (2021) 18743–18749, https://doi.org/10.1021/acsami.1c01246.
[39] W. Ping, C. Wang, Z. Lin, E. Hitz, C. Yang, H. Wang, L. Hu, Reversible short-circuit behaviors in garnet-based solid-state batteries, Adv. Energy Mater. 10 (2020) 2000702, https://doi.org/10.1002/aenm.202000702.